Nanophysical mapping of inflammasome activation by nanoparticles via specific cell surface recognition events

Cristina Lo Giudice[1,†*], Jinsung Yang[1], Mégane A. Poncin[1], Laurent Adumeau[2], Martin Delguste[1], Melanie Koehler[1], Andra C. Dumitru[1], Kenneth A. Dawson[2,3], David Alsteens[1*]

1 Louvain Institute of Biomolecular Science and Technology, Université catholique de Louvain, Louvain-la-Neuve, Belgium. 2 Centre for BioNano Interactions, School of Chemistry, University College Dublin, Dublin, Ireland. 3 Guangdong Provincial Education Department Key Laboratory of Nano-Immunoregulation Tumour Microenvironment, The Second Affiliated Hospital, Guangzhou Medical University, Guangzhou, Guangdong, China.

KEYWORDS. Atomic Force Microscopy, Silica Nanoparticles, Innate Immunity, Inflammasome, Scavenger Receptors, Force Spectroscopy.

ABSTRACT: Silica nanoparticles (SiNP) trigger a range of innate immune responses in relevant essential organs, such as the liver and the lungs. Inflammatory reactions, including NLRP3 inflammasome activation, have been linked to particulate materials, however the molecular mechanisms and key actors remain elusive. Although many receptors, including several scavenger receptors, were suggested to participate in SiNP cellular uptake, mechanistic evidence of their role on innate immunity is lacking. Here we present an atomic force microscopy-based approach to physico-mechanically map the specific interaction occurring between nanoparticles and scavenger receptor A1 (SRA1) in vitro on living lung epithelial cells. We find that SiNP recognition by SRA1 on human macrophages plays a key role in mediating NLRP3 inflammasome activation, and we identify cellular mechanical changes as clear indicators of inflammasome activation in human macrophages, greatly advancing our knowledge on the interplay among nanomaterials and innate immunity. Our single-cell, quantitative approach can be readily applied to study the binding of other nanomaterials and the testing of anti-inflammatory molecules on living cells of the innate immune system.

NLRP3 inflammasomes are multiprotein complexes controlling inflammatory responses and antimicrobial defense in stimulated immune cells[1, 2]. A first priming step by microbial exposure, typically bacterial lipopolysaccharides (LPS), upregulates inflammasome transcription, leading to increased expression levels of pro-interleukin-1β and ASC protein. Subsequently, the recognition of inflammatory ligands triggers sensor activation, recruitment, and oligomerization of apoptosis-associated speck-like (ASC) adaptor protein, which in turn modulates caspase-1 activation, interleukin-1β, and interleukin-18 secretion, and induces cell death by pyroptosis[1]. Besides the critical role of inflammasomes in infectious diseases and host defense against foreign bodies, misregulation of inflammasome has been linked to cancer, autoimmune, metabolic, and neurodegenerative diseases, thus a detailed understanding and possibly modulation of its activation is of great clinical relevance[3-5]. Amorphous nanosilica has been recently found to act as NLRP3 inflammasome activator following LPS priming in a variety of immunocompetent cells, and particularly in monocytes and macrophages[6, 7].

While some general trends associating inflammasome activation to nanoparticle size and surface chemistry have started to emerge[8-10], few studies focused on the very first steps of the SiNP interaction with the macrophage biological machinery[11]. The resulting lack of mechanistic insights hampers de facto, on the one hand, comprehensive health risk assessment[12], and on the other hand the interesting perspective of modulating the interplay between nanosilica and innate immunity for therapeutic purposes. It has been widely reported that in physiologically relevant conditions, nanomaterials are mostly uptaken by the cell surface machinery through energy-driven processes, indicating the involvement of receptors in nanomaterial recognition[13, 14]. Cell surface receptors typically expressed in monocytes and macrophages include Toll-like receptors (TLRs), Fc receptors (FcRs), and scavenger receptors (SRs)[15]. While TLRs seem to play a role in the priming step, recent studies point toward the involvement of SRs in nanomaterials recognition in a variety of cell lines, suggesting a possible mediating role of SRs on silica nanoparticle uptake and triggering of the NLRP3 inflammasome activation cascade[11, 16-18].

Here, we use FD-based AFM to investigate, at the single nanoparticle level, the specificity and binding kinetics of silica nanoparticle recognition by SRs, focusing on scavenger receptor A1 (SRA1), on model substrates and living mammalian cells. With its piconewton force sensitivity and (sub)nanometer spatial resolution, together with the capability of operating in a liquid environment and at physiological temperature, FD-based AFM has proven to be one of the most powerful tools to image and quantify receptor-ligand bonds at the single-molecule and single-cell level[19-21], and to elucidate the first steps of viruses and pathogen infections[22]. Interestingly, applications of FD-based AFM and

related techniques to the field of nanomedicine and nanotoxicology are still quite limited[23-25]. Here, we applied FD-based AFM to the investigation of nanoparticle-receptors and cell interactions, and we further used AFM and confocal microscopy to investigate mechanical changes and NLRP3 inflammasome activation in macrophage-differentiated human monocytes in normal conditions and impaired nanoparticle-SRA1 interactions. Our results indicate a highly specific, avidity-based mechanism of SiNP-SRA1 interaction, which seems to play a key role in mediating NLRP3 inflammasome activation and related mechanical changes, paving the way for the use of SRs inhibitors as a possible strategy to modulate SiNP-induced inflammation.

RESULTS AND DISCUSSION

Single-nanoparticle force spectroscopy measurements on purified SRA1 receptors. To gain first insights into SiNP-SRA1 binding, we developed a platform for the study of SiNP interactions with purified SRA1 at the molecular level by single-nanoparticle AFM-based force spectroscopy. Endotoxin-free amino-functionalized SiNP (100 nm diameter) were conjugated to AFM cantilevers via heterobifunctional PEG linkers (Figure 1a,b and Figure S1). Since it is well-known that nanomaterials interactions with the biological machinery are mediated by the recruitment of biomolecules from the media (biomolecular corona)[26], SiNP-functionalized cantilevers were pre-incubated in 10% serum-supplemented cell culture media for 30 min before the measurements to mimic cell culture conditions and allow the formation of the nanoparticle biomolecular corona[27] (Figure S2). To perform force spectroscopy, SiNP-functionalized cantilevers were cyclically approached and retracted from purified SRA1-functionalized substrates, while recording the force of interaction as a function of the distance from the surface, resulting in the acquisition of force-distance curves[21] (Figure 1c). Specific bond rupture events between NPs covalently linked to AFM tip and immobilized receptors on the surface are characterized by a non-linear stretching profile compatible with the extension of the PEG linker before receptor-ligand bond rupture (Figure 1c). In 8.4 ± 3.0 % (N=9) of the total curves recorded on 5 x 5 μm^2 areas, specific unbinding events are observed (Figure 1d) corresponding to interactions between the SiNP attached onto the AFM tip and SRA1 receptors bound to the surface. To confirm the specificity of the interaction, we performed a receptor blocking assay with a monoclonal antibody directed against SRA1, and observed a significant decrease of the binding probability (BP: 3.4 ± 2.6 %), confirming that the observed unbinding events are effectively the result of SiNP-SRA1 bond ruptures when retracting the AFM tip (Figure 1d).

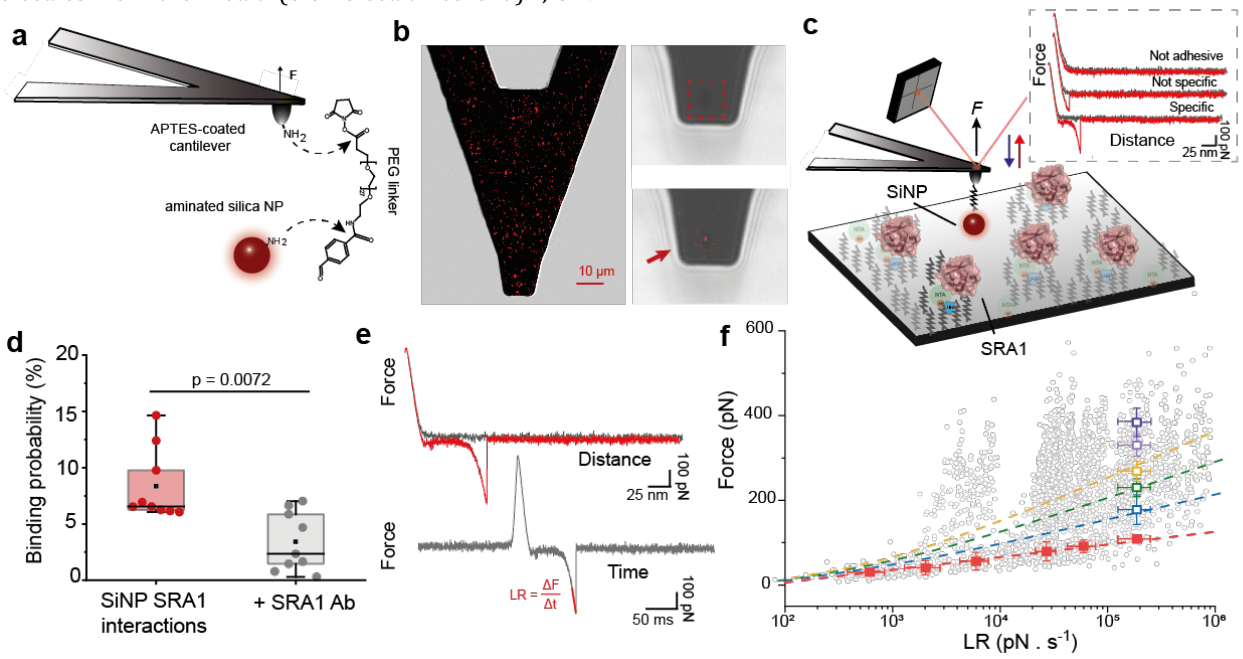

Figure 1. Probing SiNP binding to purified SRA1. (a) Schematics of covalent functionalization of AFM cantilevers with 100 nm aminated SiNP. (b) Confocal microscopy characterization of AFM cantilevers functionalized with Cy5-labeled SiNP. 2D projection of a Z-stack of the whole cantilever (left), and zoomed images of the focal plane of the tip (right, PMT channel on top image, and overlap of PMT and Cy5 channel on bottom image). (c) Schematic representation of the experimental setup. Purified SRA1 are immobilized on model surfaces through His-Tag-Ni-NTA chemistry. Inset: representative FD curves examples. (d) Binding probability of nanoparticle to SRA1 in the absence (pink) and presence (grey) of a monoclonal antibody directed against SRA1 (SRA1 Ab) (Mann Whitney test). The number of points (N =9) indicates the number of AFM maps recorded. Box plot shows mean (white dot), median (–), 25th, and 75th percentiles (boxes), and ranges from min to max (whiskers) (e) Representative FD curve of SiNP-SRA1 unbinding event (red) and corresponding force versus time curve, showing LR analysis (grey). (f) Rupture force versus LR plot of SiNP-SRA1 interactions. Bell-Evans fit (red line) and William-Evans prediction for multiple parallel bonds (blue, green, and yellow line for 2, 3, and 4 bonds respectively) are overlaid. Dots show the most probable rupture forces for single bonds (red dots) and multiple order bonds (blue, green, yellow, violet, and purple for order 2-5 respectively), as extrapolated from the multi-Gaussian fit of the rupture event distributions for LR#6 range (Figure S3). The data are representative of n = 6 independent experiments. N = 2400 FD curves.

To explore the kinetics of the interaction, we force-probed the interactions at various loading rates (LR), i.e. the rate at which the bond is stressed[21] (Figure 1e,f). The rupture forces of the SiNP-SRA1 unbinding events are then plotted as a function of the LR and analyzed through discrete ranges of LR as previously described[28]In each LR range, a variety of rupture events at multiple forces is observed. The rupture events at lower forces correspond to single order interactions between NP and SRA1, while at higher forces multiple order interactions are observed, likely corresponding to interactions of SiNP with multiple SRA1 molecules and SiNP interactions with multiple regions of the same receptor[28].

Interestingly, for the single-bond rupture, we found a linear relationship between the rupture force and logarithm of the LR (Figure 1f). According to the Bell-Evans model[29], the SiNP-SRA1 interaction can be described as a simple two-state model, in which the bound state is separated from the unbound state by a single energy barrier located at distance $x_u = 0.32 \pm 0.01$ nm and crossed with a transition rate of $k_{off} = 4.8 \pm 0.5\ s^{-1}$ (corresponding to a bond lifetime τ of 0.2 s), which indicates a rather short-lived bond compared to other ligand-receptor couples, such as viruses-cell membrane receptors[22, 28]. For the lower LR (LR ranges 1-5), the multivalent components obtained by the Williams-Evans prediction are so close that deconvolution of the raw data is not straightforward. However, for the LR range #6, we observed a good agreement between the raw data distribution and the William-Evans prediction for n-order parallel uncorrelated bonds (Figure 1f and Figure S3). Furthermore, high-order interactions are observed with remarkable frequency, representing ≈ 58% of the total fraction of binding events and ≈ 81% of the binding events in the LR ranges #3-6. The relative labile kinetics of the first order SiNP-SRA1 bond, together with the high abundance of multiple bonds, previously observed for viruses[28], suggests that the stability of SiNP-SRA1 interactions would rely mostly on nanoparticle avidity, as opposed to ligand-receptor affinity.

Overall, the data indicate that SRA1 interacts with SiNP in a specific manner and that avidity is mainly responsible for the interaction, with the formation of multiple bonds compensating for the relatively low stability of the single interactions. An avidity-based interaction mechanism reflects both the lack of high-affinity biorecognition motifs on the SiNP surface, as opposed to other biological interactions such as antibody-antigen, and the propensity of SRs for the biorecognition of a wide range of ligands, from modified forms of low-density lipoproteins to apoptotic cells and microbial ligands[30].

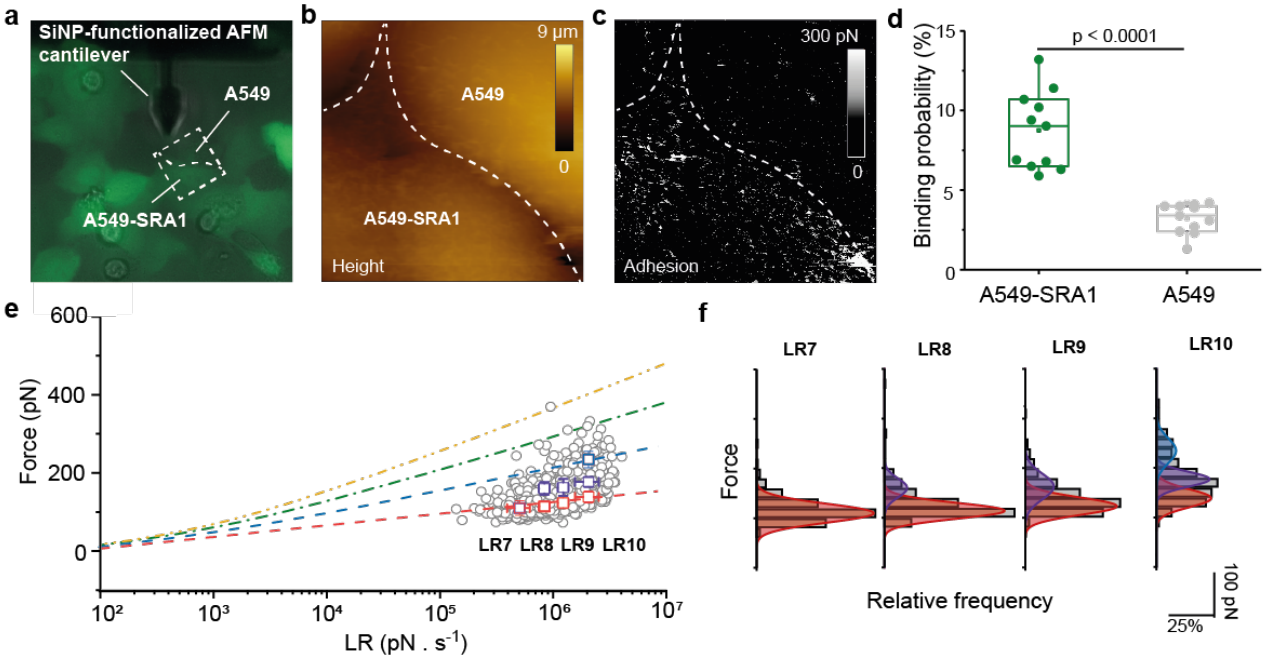

Figure 2. Mapping SiNP binding to A549-SRA1 cells using correlative optical microscopy and FD-based AFM. (a) Epifluorescence image showing co-cultures of wild-type (A549) and transduced A549 cells overexpressing eGFP-labeled SRA1 (A549-SRA1, green). The square indicates the AFM scanned area in b-c. b-c) AFM topography (b) and adhesion image (c) of adjacent A549-SRA1 and A549 cells. (d) Box plot showing the binding probability of SiNP on A549-SRA1 and A549 (two-tailed t-test). The number of points (N =11) indicates the number of AFM maps recorded. Box plot shows mean (white dot), median (–), 25th and 75th percentiles (boxes), and ranges from min to max (whiskers) The data are representative of n = 3 independent experiments. (e) Force versus LR plot showing the overlap of most probable unbinding events found on A549-SRA1 (subdivided in LR#7-10) with Bell-Evans fit for the single SiNP-SRA1 interaction shown in Figure 1f. The data are representative of n = 3 independent experiments. N = 1206 FD curves. (f) Frequency histograms of A549-SRA1 bond rupture events (LR#7-10).

Probing SiNP-SRA1 interactions on living lung epithelial cells. After having demonstrated the specific binding on purified receptors, we assessed the SiNP binding to SRA1 on living mammalian cells. This allowed us to characterize the interactions in physiologically relevant conditions and confirm the specificity of the interaction in a more complex environment, i.e. in presence of a variety of other exposed cell surface receptors and glycans. Lung epithelial A549-cells were transduced to overexpress green fluorescently labeled SRA1 receptors (A549-SRA1), cocultured together with wild-type A549 cells, and imaged using an epifluorescence microscope coupled to an AFM setup (Figure 2a)FD-based AFM in off-resonance tapping mode enabled the simultaneous acquisition of cell topography and SiNP binding properties at high resolution. By scanning adjacent transduced and not transduced A549 cells with the SiNP functionalized tip, we found a significantly higher frequency of SiNP binding events on A549-SRA1 cells (BP: 8.6 ± 3.2%) compared to control cells (BP: 3.0 ± 1.0 %) (Figure 2b-d). Upon extraction and analysis of the SiNP bond rupture events, we confirmed that the most probable rupture forces for the single SiNP-SRA1 interaction on living cells show very good correspondence with the Bell-Evans fit obtained on purified receptors, confirming specific SiNP-SRA1 interactions on living cells (Figure 2e,f). However, we also found a population of forces (purple) at intermediate values between the SRA1 single- (red) and double interactions (blue), probably corresponding to spurious interactions of SiNP with other receptors or other biomolecules, such as glycans. The generally lower abundance of high-order interactions observed in the cell experiments compared to the purified receptors is to be ascribed to the shorter nanoparticle-receptor contact time experienced in peak-force tapping mode compared to force-volume mode, which reduces the probability of successful bond establishment.

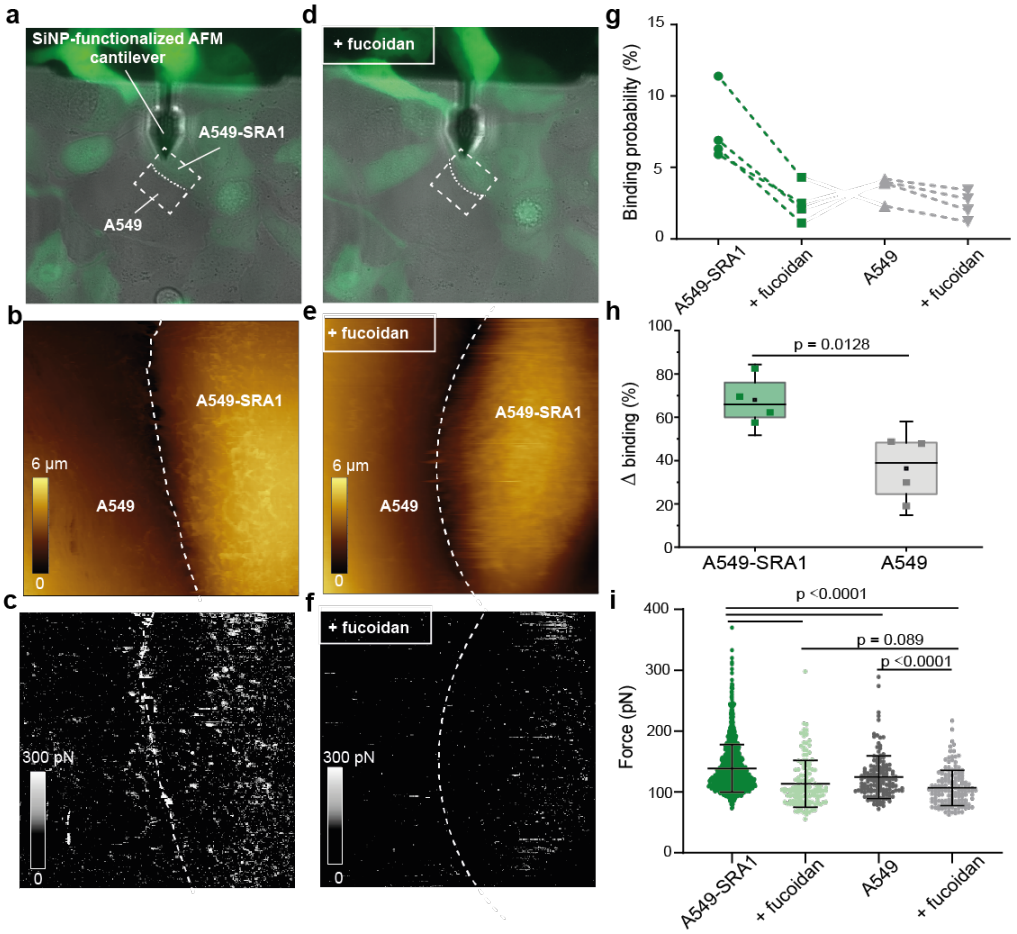

Figure 3. Specificity of SiNP SRA1 recognition on living A549-SRA1 cells (a) Epifluorescence image showing co-cultures of A549 cells (unlabeled) and transduced A549 cells overexpressing eGFP-labeled SRA1 (A549-SRA1, green). The dashed square indicates the AFM scanned area in b-c (45 degrees rotation). b-c) AFM topography (b) and adhesion image (c) of adjacent A549-SRA1 and A549 cells. (d-f) Epifluorescence image (d), AFM topography (e), and adhesion image (f) of adjacent A549-SRA1 and A549 cells in a-c after 30 min incubation with 50 µg mL-1 fucoidan. (g) Binding probability before and after fucoidan competition. Each dot represents the SiNP binding probability on a single cell. The same cells have been used for binding probability estimation before and after fucoidan incubation. (h) Box plot showing the reduction of the binding probability (expressed in %) after incubation with fucoidan. Each square represents the difference in SiNP binding probability on single cells before and after fucoidan competition (two-tailed t-test). Box plot shows mean (black square), median (–), 25th and 75th percentiles (boxes), and standard deviation (whiskers). The data are representative of n = 3 independent experiments. (i) Force distributions of SiNP-A549-SRA1 interactions (dark green, N = 1206), SiNP-A549-SRA1 interactions after fucoidan incubation (light green, N = 150), SiNP-A549 interactions (dark grey, N = 150) and SiNP-A549 interactions after fucoidan incubation (light grey, N = 150) (two-tailed t-test).

To investigate the specificity of SiNP-SRA1 interactions further, we performed control experiments with fucoidan, a specific competitive ligand for class A SRs[31], (Figure 3) and we found a significant decrease of the SiNP binding probability upon fucoidan incubation for the A549-SRA1 cells (Figure 3a-g). A decrease in binding probability was also observed for the control A549 cells, again reflecting SRA1 endogenous expression. However, by comparing the normalized decrease in binding probability for the two cell lines (Figure 3h), we still found a significantly higher decrease for A549-SRA1 cells, highlighting the importance of the SRA1 receptor for SiNP recognition. We then compared the rupture force distribution of the unbinding events before and after fucoidan exposure for both A549-SRA1 and A549 cells (Figure 3i). Interestingly, while the significant difference between A549-SRA1 and A549 before fucoidan would suggest other receptors could bind SiNP with a low binding probability, in line with Figure 2d-f, the essential role of SRA1 is confirmed by evidence that fucoidan incubation alone is enough to overcome this initial statistical difference and restore natural SiNP interactions with A549 cells.

Taken together, these results suggest not only that the high specificity of SiNP-SRA1 interaction is maintained in complex biological environment but also, strikingly, that SRA1 plays a central role in nanoparticle-cell recognition.

Mechanical changes characterize inflammasome activation. As we observed a specific interaction between the SiNP and the SRA1 receptors, we further investigated whether the SRA1 SiNP recognition and subsequent uptake would play a role in SiNP-induced inflammasome activation. To this end, we used phorbol 12-myristate 13-acetate (PMA) to differentiate THP-1 cells, which expressed green-fluorescently labeled ASC protein (THP-1-ASC) as inflammasome marker[31], into macrophages (Figure 4). After PMA-induced macrophage differentiation, bacterial lipopolysaccharide (LPS) priming enhances ASC protein expression (diffuse green fluorescence). NLRP3 inflammasome activators subsequently trigger the formation of a micrometric ASC complex in the perinuclear region (green dots) (Figure 4a).

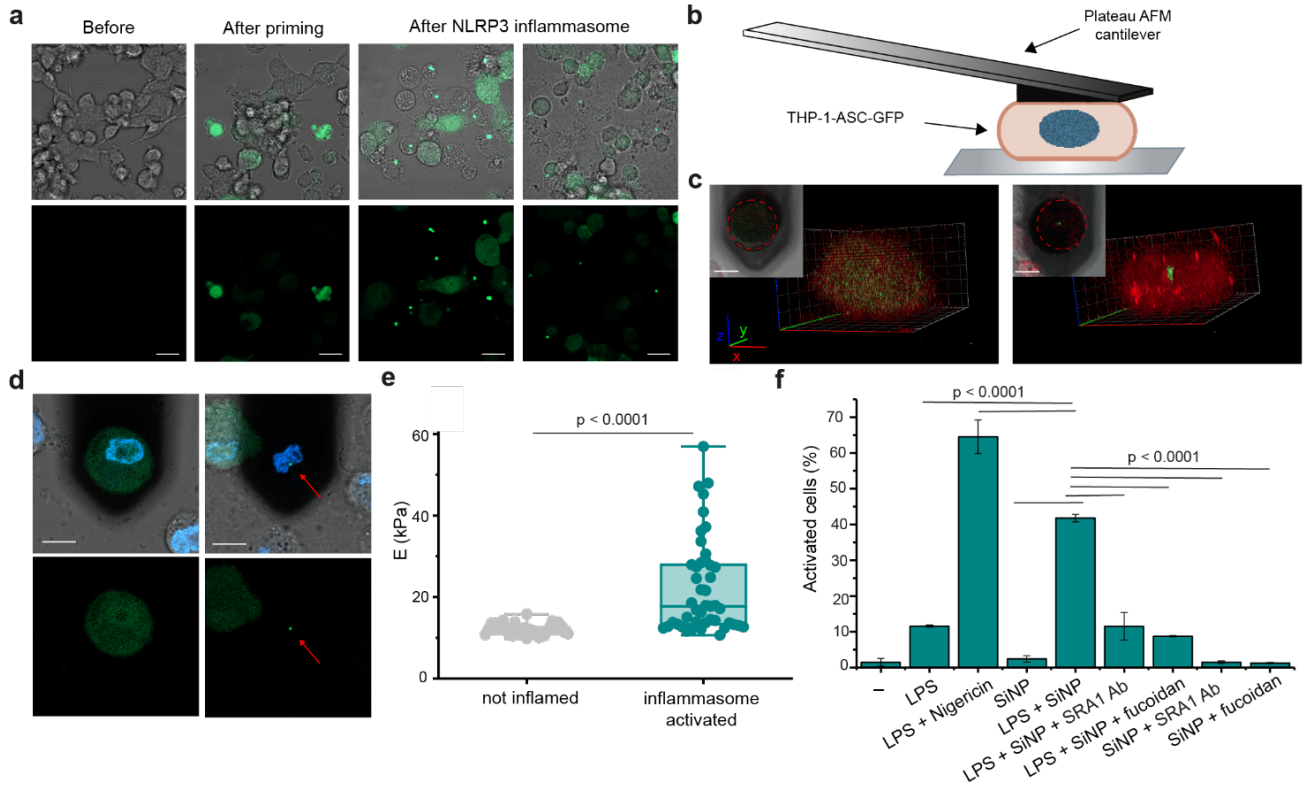

Figure 4. Mechanics of SiNP-induced inflammasome activation and role of SRA1. (a) Confocal microscopy images of macrophage-differentiated THP-1-ASC cells (PMA-treated, left), macrophage-differentiated THP-1-ASC cells after 3 h LPS priming (second left), and macrophage-differentiated THP-1-ASC cells after 3 h LPS priming and 1 h NLRP3 inflammasome activation with nigericin (second right) or SiNP (right). Scale bar 20 μm. (b) Schematics of cell mechanics AFM experiments. (c) 3D-view of CellTracker-stained LPS-primed THP-1-ASC cell (left) and NLRP3-activated cell (right) during the cell mechanics experiment with the wedged cantilevers (scale bars 3 μm). Insets show the corresponding top-views (scale bars 10 μm). (d) Top-view confocal images of Hoechst-stained THP-1-ASC cells during cell mechanics measurement: overlap of bright field, GFP (green), and Hoechst (blue) channels (top), GFP channel only (bottom) Scale bars 10 μm. (e) . Young modulus of not inflamed and NLRP3 inflammasome-activated THP-1-ASC cells (Mann-Whitney test) Each point represents the fit of a force versus indentation curve (N = 45). The data are representative of N = 9 cells per condition and n = 3 independent experiments. Box plot shows median 25th and 75th percentiles (boxes), and ranges from min to max (whiskers). (f) Comparison of several experimental conditions on THP-1-ASC cells inflammasome activation (two-tailed t-test). Data show mean ± s.d.. For each condition, an average of N = 432 ± 130 cells from 6 sample areas were analyzed. The data are representative of n = 3 independent experiments.

In our experiments, after LPS priming, we found that further incubation for 1 h with either the well-known inflammasome inducer nigericin or with SiNP results in NLRP3 inflammasome activation, as shown from the formation of ASC complexes (green dots) in Figure 4a, indicating that SiNP also acts as inflammasome activators. Besides, we observed that inflammasome activation of macrophage-differentiated THP-1-ASC cells is accompanied by a characteristic morphological change towards a granular phenotype and by loss of cell adhesions, reflecting cell transition to pyroptosis (Figure S4).

To characterize the change in THP-1 morphology observed upon NLRP3 inflammasome activation, we compared the mechanical properties of macrophage-differentiated THP-1-ASC cells in not activated and inflamed states (Figure 4b-e). To this aim, ~20 μm plateau cantilevers were placed over target primed and NLRP3-activated cells (Figure 4b,c) and used to acquire force cycles. The use of plateau cantilevers allowed us to average mechanical properties over the entire cell surface, thus avoiding local differences due to cell heterogeneity. Figure 4c shows side-view 3D reconstructions of not activated and NLRP3-activated THP-1 cells during the cell mechanics experiments, which were used to estimate cell geometrical parameters during compression. Top-view examples of not inflamed and NLRP3-activated cells are shown in Figure 4d. The force cycles for the NLRP3 inflammasome activated cells present a higher hysteresis between the approach and the retraction curve, compared to not activated cells (Figure S5). This trend is indicative of higher viscous losses, reflecting a difference in viscoelastic properties upon inflammasome activation[32]. Furthermore, upon the estimation of the cell Young modulus E from the approach part of the force versus indentation curves, we found a significant increase of E upon inflammasome activation (Figure S5 and Figure 4e). While an increase in viscous behavior has been already observed for other forms of regulated cell death, such as apoptosis, ferroptosis, and necroptosis[33], this is generally accompanied by a decrease in Young modulus[33, 34], in contract to what we observed for pyroptosis. While more investigation is needed to clarify the biological role of the probed difference in viscoelasticity, our results suggest that mechanical changes are clear indicators of inflammasome activation in human macrophage-differentiated monocytes.

SRA1 mediates SiNP-induced NLRP3 inflammasome activation. By performing co-incubation experiments, we then compared the ability of SiNP to induce the activation of the inflammasome machinery in a variety of experimental conditions, and in particular upon impairing SiNP interactions with SRA1 (Figure 4f). Strikingly, a significant reduction of the NLRP3-activated cells was found when SiNP cell exposure was conducted in presence of the SRA1 ligand fucoidan or a monoclonal antibody directed against SRA1, suggesting that SRA1 is a crucial mediator of SiNP-induced inflammasome activation.

In summary, here we developed a single-nanoparticle FD-based AFM approach which we exploited to map the biophysics and specificity of interaction between SiNP and SRA1 in biologically relevant conditions on living cells. Understanding the interplay between nanomaterials and the immune system is critical to predicting the outcome of accidental nanomaterial exposure in nanotoxicology, as well as to direct and control the biological destiny of ever-growing nanomedicine-based drugs and applications. Our approach sets up an innovative pipeline for AFM-based biophysical nano-biointeractions studies. Strikingly, the investigation of SiNP interactions with macrophage-differentiated THP-1 cells as a model of innate immunity uncovered a key role of SRA1 in mediating nanoparticle uptake-related NLRP3 inflammasome activation. We also evidenced cell mechanical changes as an indicator of inflammasome activation in living monocytes offering new perspectives for the use of AFM as diagnostic tool. Besides offering important mechanistic insights into nanoparticle-interplay with the innate immune system, our results offer interesting perspectives on the use of SRs inhibition as therapeutic strategy to reduce particulate-induced acute innate immune reactions, paving the way to further investigations in this promising therapeutic direction in the context of nanomaterials and inflammasome-related diseases. On the long run, our single-cell biophysical platform could be used to systematically test drugs, targeting specific steps of the cascade, from the initial interaction with cell membrane receptors using FD-based AFM, to more downstream signals, exploiting the combination of cell mechanics and confocal measurements. Finally, our method can be very easily transferred to other nanomaterials and biological targets, offering new perspectives in nanotoxicology, nanomedicine and nano-enabled immunomodulation.

METHODS

SiNP synthesis and characterization. The preparation of the Cy5-labeled SiNP was adapted from a procedure described previously[35, 36] and realized under sterile conditions. Briefly, a solution composed of 10.8 mL of ethanol and 120 μL of tetraethyl orthosilicate (TEOS) (Sigma Aldrich, 131903) was added to a solution containing 10.8 mL of ethanol, 57 μL of H_2O and 509 μL of Ammonia solution (35% w/w) (Fisher scientific,10111660). After 2 h, silica seeds of about 15 nm were formed. Then, 1 mL of the seed dispersion was added to a solution composed of 8.3 mL of ethanol, 2.8 mL of H_2O and 160 μL of ammonia solution, and 50 μL of TEOS as well as 50 μL of Cy5 solution were added, followed by successive addition every 30 min. In total, 1 mL of TEOS and 1 mL of Cy5 solution were added. Finally, 1.2 mL of TEOS was added in successive additions, to reach a diameter of 100 nm. 12 h after the last addition of TEOS, the dispersion was diluted by 5 with ultrapure water (Optima™ LC/MS Grade, Fisher scientific, 10505904), and the particles were washed 3 times by centrifugation.

The Cy5 solution was prepared as follow: 2 mg of Sulfo-Cyanine5 maleimide (Lumiprobe) dissolved in 40 μL of dimethyl sulfoxide (DMSO) were added to 1 mL of anhydrous methanol followed by the addition of 9 μL of a solution of (3-mercaptopropyl)trimethoxysilane (Sigma Aldrich, 175617) diluted at 10 % in methanol. The Cy5 solution was ready to use after 2 h.

Cy5-labeled SiNP were aminated as previously described[36]. Briefly, the particles were dispersed at 10 $g \cdot L^{-1}$ in a mixture of water and ethanol at a ratio 1:1, and 3-aminopropyltrimethoxysilane (Sigma Aldrich, 281778) was added at a ratio of 100 molecules/nm^2 and let stirring for 12 h. Then, a volume of glycerol, identical to the volume of water/ethanol mixture was added, and the ethanol and

water were removed by evaporation under reduced pressure at 50 °C. The particles dispersed in glycerol were then heated at 95 °C during 2 h under vacuum. The particles were washed in ethanol 4 times by centrifugation, with the addition of a few drops of acetic acid during the first washing. Particles were then stored in ethanol.

No Endotoxin contamination (0 EU) was detected in the SiNP (1g·L^{-1} in water) using the Pierce™ LAL Chromogenic Endotoxin Quantitation Kit.

Endotoxin-free, aminofunctionalised Cy5-labeled SiNP (indicated throughout the manuscript as SiNP for simplicity) were characterized by differential centrifugal sedimentation (monomer size 100 nm) and dynamic light scattering (Z average 144 nm, PDI 0.017, n = 3). The successful amination of the NP surface is confirmed by the SiNP Z-potential values of 40 mV (MES buffer 5 mM, pH 6, average of n =3 measurements). SiNP fluorescence was measured by fluorescence spectroscopy (Figure S1).

In order to characterize the SiNP hard biomolecular corona in our experimental conditions, SiNP (1 mg·mL-1 final concentration) were incubated with 10%, 30% and 50% fetal bovine serum in PBS, for 1 h at 37°C. SiNP were then washed 3 times by centrifugation at 20000 rcf, followed by resuspension in fresh PBS. After the third centrifugation steps samples were resuspended in 50 µL PBS for SDS-PAGE characterization. The SiNP-biomolecular corona complexes were denaturalized by heating the complexes in loading buffer (62.5 mM Tris-HCL pH 6.8, 2 % (w/v) SDS, 10 % glycerol, 0.01 % (w/v) bromophenol blue and 40 mM DTT) at 95°C for 5 minutes, and run on a 12% polyacrylamide gel (BioRad), under the application of a voltage of 130 V, for 1 h[14]. The gel was subsequently stained with InstantBlue (Sigma), following manufacturer's instructions. The stained gels were scanned with a (Amersham Imager 600) for visible staining and (Amersham Typhoon) for Cy5-fluorescence (Figure S2).

Cell culture and transduction. A549 cells (ATCC® CCL-185) were grown in Ham's F-12 Nutrient Mix GlutaMAX (Gibco) with 10% heat-inactivated fetal bovine serum (Gibco), 1% penicillin-streptavidin (Sigma, P4333), at 37 °C in a humidified atmosphere with 5% CO2. For transduction, cells were treated with packaged lentiviruses of pLenti-MSR1-c-GFP (ViGene Biosciences, MOI 10) in presence of Polybrene (8 µg·mL^{-1}) for 24 h. Cells successfully transduced to express GFP-labeled SRA1 receptors were selected by fluorescence activated cell sorting, using a FACS Aria instrument (BD). A549-SRA1 cells were grown in Ham's F-12 Nutrient Mix with 10% fetal bovine serum, 1% penicillin-streptavidin (Sigma, P4333) at 37 °C in a humidified atmosphere with 5% CO_2.

Human THP-1 monocytes-ASC speck GFP-labeled reporter cells (THP-1-ASC-GFP, InvivoGen) were cultured in RPMI 1640 GlutaMAX (Gibco), supplemented with 10% heat-inactivated fetal bovine serum, 1% penicillin-streptavidin (Sigma, P4333) and Normocin (100 µg·mL^{-1}). In addition, Zeocin (100 µg·mL^{-1}) was added every other passage to maintain selection procedure. For NLRP3 inflammasome activation experiments, Test Medium containing all the above-mentioned components except for Normocin and Zeocin was used, according to the manufacturer instructions.

AFM-tip functionalization and characterization. MSCT-D and PFQNM-LC cantilevers (Bruker) were used to probe the interaction between SiNP and SRA1 on model substrates and living A549-SRA1/A549 cell cocultures respectively. N-hydroxysuccinimide (NHS)-PEG24-Ph-aldehyde linkers (BroadPharm) were used to functionalize AFM tips as previously described[37]. Briefly, the cantilevers were immersed in chloroform for 10 min and further cleaned in a UV radiation and ozone (UV-O) cleaner (Jetlight), and placed in a dessicator under Ar atmosphere together with 30 µL (3-aminopropyl)triethoxysilane (APTES) and 10 µL of triethylamine. After removal of the APTES and triethylamine trays, the AFM cantilevers were left to cure under Ar for 2 days. APTES-coated cantilevers were then immersed for 2 h in a solution prepared by mixing 3.3 mg of NHS-PEG_{24}-Ph-aldehyde linker dissolved in 0.5 mL of chloroform with 30 µL of triethylamine, then washed with chloroform and dried with nitrogen gas. The cantilevers were then placed on Parafilm (Bemis NA) in a small plastic dish, and SiNP suspension (100 µL at 10^8 particles mL^{-1} in MilliQ water) was pipetted onto the cantilevers. A freshly prepared solution of $NaCNBH_3$ (2 µL at ~6% wt. vol^{-1} in 0.1 M NaOH(aq)) was gently added to the SiNP suspension and the mixture was left in incubation for 1 h at room temperature. Then, 5 µL of 1 M ethanolamine solution (pH 8) was gently mixed into the drop to quench the unreacted aldehyde groups. SiNP-functionalized tips were stored in MilliQ water at 4°C and used within a few days.

The Cy-5-labeled-SiNP-functionalized cantilevers were characterized by laser scanning confocal microscopy and SEM. For confocal imaging, we used a Zeiss LSM-980 microscope equipped with a Plan Apo 63× numerical aperture (NA) 1.4 water immersion objective. The tips were first brought into contact with the surface of glass-bottom WillCo dishes (GWST-5040) in MilliQ water and Z-stacks images acquisition was used to reconstruct the distribution of SiNP on the AFM tip, as well as on the entire cantilever.

Preparation of purified SRA1-functionalized model substrates. Model substrates were functionalized with recombinant human SRA1 (Lys-77-Leu451 with an N-terminal His_9-tag, R&D P21757) using NTA-His tag binding chemistry. Gold-coated silicon surfaces were rinsed with ethanol, dried with a gentle nitrogen flow, cleaned for 15 min by UV and ozone treatment, and immersed overnight in ethanol containing 0.05 mM of NTA-terminated (1%) and triethylene glycol(EG)-terminated (99%) alkanethiols. After rinsing with ethanol, the samples coated with alkanethiols were immersed in a 40 mM aqueous solution of $NiSO_4$ for 30 min, rinsed with water, incubated with recombinant SRA1 (25 µL, 0.1 mg·mL^{-1} in PBS) for 1 h, and rinsed with PBS. The functionalized surfaces were kept hydrated and used immediately after preparation.

FD-based AFM on model surfaces. FD-based AFM on model substrates was performed using a JPK ForceRobot 300 instrument equipped with a high-precision stage. Before the experiments, SiNP-functionalized MSCT-D probes were preincubated in F-12 Nutrient Mix supplemented with 10% fetal bovine serum for 30 min to favor the in situ formation of the nanoparticle biomolecular corona. After 3 steps of washing by immersion of the cantilevers in PBS to gently remove the excess of unbound biomolecules, the SiNP-functionalized probes were mounted on the AFM

setup and calibrated using the thermal tune method[38]. The calibrated cantilevers were used to record force curves from 5 × 5 µm arrays in the force-volume (contact) mode. The approach velocity was kept constant at 2 µm s^{-1}, and retraction velocities were varied from 0.1, 0.2, 1, 2, 5, 10 to 20 µm s^{-1} to probe the interactions between the SiNP and SRA1 over a wide range of LRs. The pulling velocity (v) and LR can be related as follows:

$$LR=\Delta F/\Delta t=k_{eff}\cdot v \quad (1)$$

where $\Delta F/\Delta t$ being the applied force over time, and k_{eff} the effective spring constant of the system. A force setpoint of 500 pN and a ramp size of 300 nm were used, with no surface delay. The sample rate was adjusted in order to acquire 2400 data points (FD curves) per retraction speed. All FD-based AFM measurements were performed in PBS buffer at room temperature (RT).

For SRA1 blocking experiments, SRA1-functionalized model substrates were first scanned with SiNP-functionalized tips (5 × 5 µm areas, 1 µm·s^{-1} retraction speed) and then incubated with monoclonal mouse IgG recognizing Lys-77-Leu451 SRA1 domain (0.1 mg·mL^{-1}, R&D P21757), while cantilevers were removed from the surface. After 30 min incubation at RT, SiNP-functionalized tips were brought again into contact with the blocked SRA1 surfaces, and further scans were performed (5 × 5 µm areas, 1 µm·s^{-1} retraction speed).

Force curves were analyzed using the JPKSPM data analysis software. To identify specific rupture events corresponding to the interaction between SiNP linked to the PEG spacer and the receptor model surface, the retraction curve before bond rupture was fitted with the worm-like chain model for polymer extension[39]. Origin software (OriginLab) was used to display the results in force versus LR plots, to fit histograms of rupture force distributions for distinct LR ranges and to apply Bell-Evans model and the Williams-Evans multiple bond prediction, as described[28]. Briefly, force and LR were extracted from force versus time curves and sorted in discrete LR ranges (LR#1, <$1\cdot10^3$ pN · s^{-1}; LR#2, $1\cdot10^3$ to $3.5\cdot10^3$ pN · s^{-1}; LR#3, $3.5\cdot10^3$ to $1\cdot10^4$ pN · s^{-1}; LR#4, $1\cdot10^4$ to $3.5\cdot10^4$ pN · s^{-1}; LR#5, $3.5\cdot10^4$ to $1\cdot10^5$ pN · s^{-1}; LR#6, > $1\cdot10^5$ pN · s^{-1}). Frequency distributions of rupture forces were plotted for each LR range (Figure S3). Multimodal Gaussian fits were used to extract the average rupture forces for single order SiNP- SRA1 binding (first peak) and multiple order interactions for each LR range. The average rupture forces for the first order ligand-receptor interactions are used for Bell-Evans fit. Statistical analyses were performed with Prism software (Graphpad).

FD-based AFM on co-culture of A549-SRA-1/A549 cells. A Bioscope Resolve AFM setup (Bruker) equipped with a 100-µm piezoelectric scanner and coupled to an epifluorescence microscope (Zeiss Observer Z.1, 40x oil objective) was used to acquire correlative images. The setup used is equipped with a cell-culture chamber to maintain the temperature at constant values (37 ± 1 °C). To keep cells in physiologically-relevant conditions, humidified (95 ± 2% relative humidity) synthetic air (80% N_2 and 20% O_2) supplemented with 5% CO_2 was provided continuously around the cell plate allowing to diffuse into cell-culture media[28]. Fluorescence images were recorded using an oil-immersion lens (40x, NA 1.20, Zeiss C-Apochromat). After sample inspection and selection of suitable scanning regions usually including adjacent A549-SRA1 and A549 cells, SiNP-functionalized PFQNM-LC cantilevers (Bruker) were used to record AFM images (256x256 pixels, ~25 $µm^2$) at a peak force setpoint of 500 pN, 0.25 kHz peak force frequency and 750 nm amplitude, using PeakForce Tapping mode (Bruker). Force curves were analyzed using the Nanoscope data analysis software. Origin software (OriginLab) was used to display the results in force versus LR plots and to fit histograms of rupture force distributions for distinct LR ranges (LR#7 < $6.75\cdot10^5$ pN · s^{-1}; LR#8 $6.75\cdot10^5$ to $1\cdot10^6$ pN · s^{-1}, LR#9 $1\cdot10^6$ to $1.5\cdot10^6$ pN · s^{-1}, LR#10 > $1.5\cdot10^6$ pN · s^{-1}), as described in the model surfaces section.

For ligand competition experiments, after scanning of adjacent A549-SRA1 and A549 cells, fucoidan was spiked into the cell media (50 µg·mL^{-1} final concentration[31]) and allowed to bind for 30 min, after which the SiNP-functionalized cantilevers were brought again contact with the cell samples and previously imaged sample regions were imaged again for direct comparison of SiNP-SRA1 interaction before and after competition ligand binding.

Epifluorescence images and AFM scans were visualized using Zen software (Zeiss) and Nanoscope Analysis software (Bruker), respectively. ImageJ software was used to quantify the SiNP binding probability from AFM adhesion images. Statistical analyses were performed with Prism software (Graphpad).

Differentiation and NLRP3 inflammasome activation experiments. For macrophage-differentiation, $1\cdot10^6$ THP-1-ASC-GFP cells were seeded in glass-bottom WillCo dishes (GWST-5040) and incubated with phorbol 12-myristate 13-acetate (PMA, 5 ng·mL^{-1} final concentration[40]) in growth medium for 24 h, after which cells were washed twice with PBS and incubated with fresh medium for further 24 h in order to let them recover from the PMA treatment before NLRP3 inflammasome activation assays. Successful PMA-induced differentiation resulted in the THP-1 cells transitioning from the non-adherent phenotype typical from monocytes to adherent macrophage-like phenotype.

NLRP3 inflammasome activation requires two steps: a priming step, usually triggered by lipopolysaccharade (LPS) exposure, which induces NF-κB-mediated NLRP3 and pro-IL-1β expression, and the activation step promoting inflammasome assembly, caspase-1-mediated IL-1β and IL-18 secretion and pyroptosis[1]. Preliminary experiments to validate the cell line and optimize the assay were performed by incubating differentiated THP-1-ASC-GFP cells with LPS (10 ng·mL^{-1})31 for 3 h at 37°C in 5% CO_2 (priming), followed 1 h incubation with Nigericin (10 µM) or SiNP (~10^{10} NP·mL^{-1}) (Figure 4A). Cell fluorescence was monitored in situ, using a Zeiss LSM-980 confocal microscope equipped with a Plan Apo 63× numerical aperture (NA) 1.4 water immersion objective.

For the NLRP3 inflammasome activation experiments reported in Figure 4F, PMA-differentiated THP-1-ASC-GFP cells were co-incubated for 3 h at 37°C in 5% CO_2 with the primer (LPS, 10 ng·mL^{-1}) and either SiNP (~10^{10} NP·mL^{-1}), SiNP (~10^{10} NP·mL^{-1}) in presence of SRA1 blocking antibody (0.01 mg·mL^{-1}, R&D P21757), or SiNP (~10^{10} NP·mL^{-1}) in presence of fucoidan (50 µg·mL^{-1}), after which samples were fixed with 3.7% paraformaldehyde for 15 min, washed twice with PBS and stored in the fridge until confocal analysis. Co-incubation with (LPS, 10 ng·mL^{-1}) and Nigericin (10

μM) was used as positive control, while differentiation only (PMA exposure), incubation with LPS (10 ng·mL^{-1}), and incubation with SiNP only (65 μg·mL^{-1}) were used as negative controls.

Cell mechanics measurements. For cell mechanics measurements, custom-made cantilevers with a 21-23 μm plateau tip (5 N·m^{-1} spring constant, 125 mm length, 30 μm width, 2 μm thickness) were purchased by NuNano, UK. The plateau cantilevers were calibrated with the thermal tune method, and brought into contact with either not inflamed or inflammasome-activated THP-1-ASC-GFP cells. FD curves were acquired in contact mode, using 100 nN force setpoint, 5 μm ramp size, and 25 μm·s^{-1} approach and retraction velocities, corresponding to 2.54 Hz ramp frequency. AtomicJ software was used to process and analyze the data, using the Robust golden model for contact point estimation and the blunt cone model for the determination of E. For cell contact radius r estimation, THP-1-ASC-GFP cells were labeled with cytosolic Cell trackerTM Deep red dye (ThermoFisher C34565) following manufacturer's instructions, approached by the plateau cantilevers and imaged by confocal microscopy, leading to r = 9.6 ± 0.9 μm. Poisson ratio was set to 0.5 and E was calculated using the approach part of the force cycle to avoid adhesion and viscosity artefacts. Statistical analyses were performed with Prism software (Graphpad).

ASSOCIATED CONTENT

Supporting Information. SiNP characterization by DLS, differential centrifugal sedimentation and fluorescence spectroscopy. SDS-PAGE showing SiNP hard corona in FBS. Rupture forces frequency distributions of the binding events. Zoomed images showing PMA-differentiated THP-1 cells. Representative force-distance and force versus indentation curves for cell mechanics experiment. This material is available free of charge via the Internet at http://pubs.acs.org."

AUTHOR INFORMATION

Corresponding Authors

* Email: david.alsteens@uclouvain.be
* Email: cristina.logiudice@uclouvain.be.

Present Addresses

†Cellular Biophysics Department, Max Planck Institute for Medical Research, Heidelberg, Germany

Author Contributions

CLG and DA designed the study. CLG performed all the experiments, data analysis and interpretation. JY and MP helped with A549 and THP1-ASC-GFP cell handling and experiments. LA and KD provided Cy5-labeled endotoxin-free SiNP. MD assisted with the characterization of SiNP-functionalized cantilevers. MK and AD trained CLG in FD-based AFM. The manuscript was written through contributions of all authors.

Funding Sources

This work was supported by the Université catholique de Louvain and the Fonds National de la Recherche Scientifique (F.R.S.-FNRS; PDR T.0070.16 to D.A.) and by the European Molecular Biology Organization (EMBO) (ALTF 542-2018 to C.L.). D.A. is a Research Associate at the FNRS

ACKNOWLEDGMENT

The authors acknowledge Prof. François Huaux at Université catholique de Louvain for the initial scientific discussions, Ms Marie-Christine Eloy for the great help with confocal and epifluorescence microscopy, and Mr François Tickaert for the assistance with the Cell-tracker experiment.

ABBREVIATIONS

AFM, atomic force microscopy; SiNP, silica nanoparticles; SRA1, scavenger receptor A1; LR, loading rate; BP, binding probability.

REFERENCES

1. Broz, P.; Dixit, V. M., Inflammasomes: mechanism of assembly, regulation and signalling. Nature Reviews Immunology 2016, 16 (7), 407-420.
2. Swanson, K. V.; Deng, M.; Ting, J. P. Y., The NLRP3 inflammasome: molecular activation and regulation to therapeutics. Nature Reviews Immunology 2019, 19 (8), 477-489.
3. Zahid, A.; Li, B.; Kombe, A. J. K.; Jin, T.; Tao, J., Pharmacological Inhibitors of the NLRP3 Inflammasome. Frontiers in Immunology 2019, 10 (2538).
4. Lee, C.; Do, H. T. T.; Her, J.; Kim, Y.; Seo, D.; Rhee, I., Inflammasome as a promising therapeutic target for cancer. Life Sciences 2019, 231, 116593.
5. Voet, S.; Srinivasan, S.; Lamkanfi, M.; van Loo, G., Inflammasomes in neuroinflammatory and neurodegenerative diseases. EMBO Molecular Medicine 2019, 11 (6), e10248.
6. Bianchi, M. G.; Chiu, M.; Taurino, G.; Ruotolo, R.; Marmiroli, N.; Bergamaschi, E.; Cubadda, F.; Bussolati, O., Pyrogenic and Precipitated Amorphous Silica Nanoparticles Differentially Affect Cell Responses to LPS in Human Macrophages. Nanomaterials (Basel) 2020, 10 (7).
7. Gómez, D. M.; Urcuqui-Inchima, S.; Hernandez, J. C., Silica nanoparticles induce NLRP3 inflammasome activation in human primary immune cells. Innate Immun 2017, 23 (8), 697-708.
8. Wang, J.; Chen, H.-J.; Hang, T.; Yu, Y.; Liu, G.; He, G.; Xiao, S.; Yang, B.-r.; Yang, C.; Liu, F.; Tao, J.; Wu, M. X.; Xie, X., Physical activation of innate immunity by spiky particles. Nature Nanotechnology 2018, 13 (11), 1078-1086.
9. Pavan, C.; Santalucia, R.; Leinardi, R.; Fabbiani, M.; Yakoub, Y.; Uwambayinema, F.; Ugliengo, P.; Tomatis, M.; Martra, G.; Turci, F.; Lison, D.; Fubini, B., Nearly free surface silanols are the critical molecular moieties that initiate the toxicity of silica particles. Proceedings of the National Academy of Sciences 2020, 117 (45), 27836.
10. Uemura, E.; Yoshioka, Y.; Hirai, T.; Handa, T.; Nagano, K.; Higashisaka, K.; Tsutsumi, Y., Relationship between size and surface modification of silica particles and enhancement and suppression of inflammatory cytokine production by lipopolysaccharide- or peptidoglycan-stimulated RAW264.7 macrophages. Journal of Nanoparticle Research 2016, 18 (6), 165.
11. Nishijima, N.; Hirai, T.; Misato, K.; Aoyama, M.; Kuroda, E.; Ishii, K. J.; Higashisaka, K.; Yoshioka, Y.; Tsutsumi, Y., Human Scavenger Receptor A1-Mediated Inflammatory Response to Silica Particle Exposure Is Size Specific. Front Immunol 2017, 8, 379.
12. Sharma, N.; Jha, S., Amorphous nanosilica induced toxicity, inflammation and innate immune responses: A critical review. Toxicology 2020, 441, 152519.

13. Dawson, K. A.; Yan, Y., Current understanding of biological identity at the nanoscale and future prospects. Nat Nanotechnol 2021, 16 (3), 229-242.
14. Lara, S.; Alnasser, F.; Polo, E.; Garry, D.; Lo Giudice, M. C.; Hristov, D. R.; Rocks, L.; Salvati, A.; Yan, Y.; Dawson, K. A., Identification of Receptor Binding to the Biomolecular Corona of Nanoparticles. ACS Nano 2017, 11 (2), 1884-1893.
15. Taylor, P. R.; Martinez-Pomares, L.; Stacey, M.; Lin, H. H.; Brown, G. D.; Gordon, S., Macrophage receptors and immune recognition. Annu Rev Immunol 2005, 23, 901-44.
16. Alnasser, F.; Castagnola, V.; Boselli, L.; Esquivel-Gaon, M.; Efeoglu, E.; McIntyre, J.; Byrne, H. J.; Dawson, K. A., Graphene Nanoflake Uptake Mediated by Scavenger Receptors. Nano Letters 2019, 19 (2), 1260-1268.
17. Shannahan, J. H.; Bai, W.; Brown, J. M., Implications of scavenger receptors in the safe development of nanotherapeutics. Receptors Clin Investig 2015, 2 (3), e811.
18. Tsugita, M.; Morimoto, N.; Tashiro, M.; Kinoshita, K.; Nakayama, M., SR-B1 Is a Silica Receptor that Mediates Canonical Inflammasome Activation. Cell Rep 2017, 18 (5), 1298-1311.
19. Lo Giudice, C.; Dumitru, A. C.; Alsteens, D., Probing ligand-receptor bonds in physiologically relevant conditions using AFM. Anal Bioanal Chem 2019, 411 (25), 6549-6559.
20. Lo Giudice, C.; Zhang, H.; Wu, B.; Alsteens, D., Mechanochemical Activation of Class-B G-Protein-Coupled Receptor upon Peptide–Ligand Binding. Nano Letters 2020, 20 (7), 5575-5582.
21. Müller, D. J.; Dumitru, A. C.; Lo Giudice, C.; Gaub, H. E.; Hinterdorfer, P.; Hummer, G.; De Yoreo, J. J.; Dufrêne, Y. F.; Alsteens, D., Atomic Force Microscopy-Based Force Spectroscopy and Multiparametric Imaging of Biomolecular and Cellular Systems. Chem Rev 2020.
22. Koehler, M.; Petitjean, S. J. L.; Yang, J.; Aravamudhan, P.; Somoulay, X.; Lo Giudice, C.; Poncin, M. A.; Dumitru, A. C.; Dermody, T. S.; Alsteens, D., Reovirus directly engages integrin to recruit clathrin for entry into host cells. Nat Commun 2021, 12 (1), 2149.
23. Gomes, C. P.; Oliveira, H.; Ebner, A.; Hinterdorfer, P.; Pêgo, A. P., Molecular Recognition Force Spectroscopy for Probing Cell Targeted Nanoparticles In Vitro. Methods Mol Biol 2019, 1886, 327-341.
24. Witte, A. B.; Leistra, A. N.; Wong, P. T.; Bharathi, S.; Refior, K.; Smith, P.; Kaso, O.; Sinniah, K.; Choi, S. K., Atomic Force Microscopy Probing of Receptor–Nanoparticle Interactions for Riboflavin Receptor Targeted Gold–Dendrimer Nanocomposites. The Journal of Physical Chemistry B 2014, 118 (11), 2872-2882.
25. Kolodziejczyk, A. M.; Sokolowska, P.; Zimon, A.; Grala, M.; Rosowski, M.; Siatkowska, M.; Komorowski, P.; Walkowiak, B., Dysfunction of endothelial cells exposed to nanomaterials assessed by atomic force spectroscopy. Micron 2021, 145, 103062.
26. Lo Giudice, M. C.; Herda, L. M.; Polo, E.; Dawson, K. A., In situ characterization of nanoparticle biomolecular interactions in complex biological media by flow cytometry. Nat Commun 2016, 7 (1), 13475.
27. Monopoli, M. P.; Åberg, C.; Salvati, A.; Dawson, K. A., Biomolecular coronas provide the biological identity of nanosized materials. Nature Nanotechnology 2012, 7 (12), 779-786.
28. Alsteens, D.; Newton, R.; Schubert, R.; Martinez-Martin, D.; Delguste, M.; Roska, B.; Müller, D. J., Nanomechanical mapping of first binding steps of a virus to animal cells. Nat Nanotechnol 2017, 12 (2), 177-183.
29. Merkel, R.; Nassoy, P.; Leung, A.; Ritchie, K.; Evans, E., Energy landscapes of receptor–ligand bonds explored with dynamic force spectroscopy. Nature 1999, 397 (6714), 50-53.
30. Canton, J.; Neculai, D.; Grinstein, S., Scavenger receptors in homeostasis and immunity. Nature Reviews Immunology 2013, 13 (9), 621-634.
31. Fernandes-Alnemri, T.; Wu, J.; Yu, J. W.; Datta, P.; Miller, B.; Jankowski, W.; Rosenberg, S.; Zhang, J.; Alnemri, E. S., The pyroptosome: a supramolecular assembly of ASC dimers mediating inflammatory cell death via caspase-1 activation. Cell Death Differ 2007, 14 (9), 1590-604.
32. Brückner, B. R.; Nöding, H.; Janshoff, A., Viscoelastic Properties of Confluent MDCK II Cells Obtained from Force Cycle Experiments. Biophysical Journal 2017, 112 (4), 724-735.
33. Van der Meeren, L.; Verduijn, J.; Krysko, D. V.; Skirtach, A. G., AFM Analysis Enables Differentiation between Apoptosis, Necroptosis, and Ferroptosis in Murine Cancer Cells. iScience 2020, 23 (12), 101816.
34. Su, X.; Zhang, L.; Kang, H.; Zhang, B.; Bao, G.; Wang, J., Mechanical, nanomorphological and biological reconstruction of early-stage apoptosis in HeLa cells induced by cytochalasin B. Oncol Rep 2019, 41 (2), 928-938.
35. Adumeau, L.; Genevois, C.; Roudier, L.; Schatz, C.; Couillaud, F.; Mornet, S., Impact of surface grafting density of PEG macromolecules on dually fluorescent silica nanoparticles used for the in vivo imaging of subcutaneous tumors. Biochim Biophys Acta Gen Subj 2017, 1861 (6), 1587-1596.
36. Reinhardt, N.; Adumeau, L.; Lambert, O.; Ravaine, S.; Mornet, S., Quaternary Ammonium Groups Exposed at the Surface of Silica Nanoparticles Suitable for DNA Complexation in the Presence of Cationic Lipids. The Journal of Physical Chemistry B 2015, 119 (21), 6401-6411.
37. Ebner, A.; Hinterdorfer, P.; Gruber, H. J., Comparison of different aminofunctionalization strategies for attachment of single antibodies to AFM cantilevers. Ultramicroscopy 2007, 107 (10-11), 922-7.
38. Butt, H. J.; Jaschke, M., Calculation of thermal noise in atomic force microscopy. Nanotechnology 1995, 6 (1), 1-7.
39. Bustamante, C.; Marko, J. F.; Siggia, E. D.; Smith, S., Entropic elasticity of lambda-phage DNA. Science 1994, 265 (5178), 1599-600.
40. Park, E. K.; Jung, H. S.; Yang, H. I.; Yoo, M. C.; Kim, C.; Kim, K. S., Optimized THP-1 differentiation is required for the detection of responses to weak stimuli. Inflammation Research 2007, 56 (1), 45-50.Word Style "TF_References_Section").

Insert Table of Contents artwork here